Research Article

NMR IN BIOMEDICINE

Received: 26 October 2011, Revised: 9 March 2012, Accepted: 3 April 2012, Published online in Wiley Online Library: 2012

(wileyonlinelibrary.com) DOI: 10.1002/nbm.2812

The role of gray and white matter segmentation in quantitative proton MR spectroscopic imaging

Assaf Tal, Ivan I. Kirov, Robert I. Grossman and Oded Gonen*

Since the brain's gray matter (GM) and white matter (WM) metabolite concentrations differ, their partial volumes can vary the voxel's ^{1}H MR spectroscopy (^{1}H-MRS) signal, reducing sensitivity to changes. While single-voxel ^{1}H-MRS cannot differentiate between WM and GM signals, partial volume correction is feasible by MR spectroscopic imaging (MRSI) using segmentation of the MRI acquired for VOI placement. To determine the magnitude of this effect on metabolic quantification, we segmented a 1-mm^3 resolution MRI into GM, WM and CSF masks that were co-registered with the MRSI grid to yield their partial volumes in approximately every 1 cm^3 spectroscopic voxel. Each voxel then provided one equation with two unknowns: its *i*- metabolite's GM and WM concentrations C_i^{GM}, C_i^{WM}. With the voxels' GM and WM volumes as independent coefficients, the over-determined system of equations was solved for the global averaged C_i^{GM} and C_i^{WM}. Trading off local concentration differences offers three advantages: *(i)* higher sensitivity due to combined data from many voxels; *(ii)* improved specificity to WM versus GM changes; and *(iii)* reduced susceptibility to partial volume effects. These improvements made no additional demands on the protocol, measurement time or hardware. Applying this approach to 18 volunteered 3D MRSI sets of 480 voxels each yielded *N*-acetylaspartate, creatine, choline and *myo*-inositol C_i^{GM} concentrations of 8.5 ± 0.7, 6.9 ± 0.6, 1.2 ± 0.2, 5.3 ± 0.6mM, respectively, and C_i^{WM} concentrations of 7.7 ± 0.6, 4.9 ± 0.5, 1.4 ± 0.1 and 4.4 ± 0.6mM, respectively. We showed that unaccounted voxel WM or GM partial volume can vary absolute quantification by 5–10% (more for ratios), which can often double the sample size required to establish statistical significance. Copyright © 2012 John Wiley & Sons, Ltd.

Keywords: segmentation; gray matter; white matter; spectroscopic quantification MRS

INTRODUCTION

Proton MR spectroscopy (^{1}H-MRS) provides unique specificity to pathological processes in the brain by quantifying metabolic surrogates such as: *N*-acetylaspartate (NAA) for neuronal integrity; creatine (Cr) for glial proliferation; choline (Cho) for membrane turnover; and *myo*-inositol (*m*I) for astrogliosis (1,2). Its sensitivity to their concentration changes, however, is low mainly due to: *(i)* The intrinsic low voxel signal-to-noise ratios (SNR) that reduce its reproducibility (3,4); *(ii)* variations in cerebrospinal fluid, white and gray matter (CSF, WM, GM) composition in each voxel. Since metabolite concentrations in GM differ from WM with virtually none in the CSF (5), and since pathologies may affect these tissue types differently (6,7), variations in the voxel compositions diminish the statistical power to detect changes (8). These partial volume effects are exacerbated by volume of interest (VOI) misregistration in longitudinal and cross-sectional studies.

Unfortunately, these SNRs and partial volume effect issues are inextricable. For a given instrumental setup and scan time, addressing the SNR by increasing voxel size comes at the expense of larger partial volumes and vice versa (9,10). Furthermore, the thin 1–4 mm tortuous GM ribbon (11) makes it difficult to place the ~ $2 \times 2 \times 2$ cm^3 typical single-voxel ^{1}H-MRS volumes in "pure" WM and therefore almost impossible to obtain "pure" GM voxels. In addition, single-voxel ^{1}H-MRS precludes verification of diffuse (multi-focal) metabolic changes that characterize common neurological disorders (1,2). Surprisingly, even though multi-voxel ^{1}H MR spectroscopic imaging (^{1}H-MRSI) can yield much higher (~ 1 cm^3) spatial resolution, its analysis is often done on a voxel-by-voxel basis (12) and the consequences of tissue partial volume on its precision (reproducibility) are to the best of our knowledge not discussed in the literature.

The misregistration, SNR and partial volume issues can be substantially reduced by combining absolute ^{1}H-MRSI metabolic quantification with anatomical high-spatial resolution (~ 1 mm^3) MRI that accompanies it. Using freely available segmentation software, WM/GM/CSF masks can be produced and overlaid on the ^{1}H-MRSI grid to yield their contents in each voxel (13,14). This information can yield global WM and GM metabolite concentrations by modeling the ^{1}H-MRSI signal from each voxel as a linear combination of their contributions. Thus, at the cost of averaging out regional metabolic variations (15) - a reasonable tradeoff in diffuse disorders - analysis of all voxels can dramatically improve

* *Correspondence to: O. Gonen, Department of Radiology, New York University School of Medicine, New York, 660 First Avenue, 4th Floor, New York, New York 10016, USA E-mail: oded.gonen@nyumc.org*

A. Tal, I. I. Kirov, R. I. Grossman, O. Gonen
Department of Radiology, New York University School of Medicine, New York, 660 First Avenue, 4th Floor, New York, New York 10016, USA

Abbreviations used: *GM, gray matter; WM, white matter; CSF, cerebrospinal fluid; MRSI, magnetic resonance spectroscopic imaging; SPM, statistical parametric mapping; VOI, volume of interest; FWHM, full-width at half-maximum; CSI, chemical shift imaging; NAA, N-Acetyl-Aspartate; Cho, choline; Cr, creatine; mI, myo-inositol.*

SNR while also accounting for partial volume effects. In this paper, we show that this approach improves sensitivity to diffuse/global differences that predominate in either WM or GM and estimate the metabolite concentration variations that can occur when GM and WM partial volumes are not accounted for.

MATERIALS AND METHODS

Human subjects

Eighteen (12 women, 6 men; range 19–57 y) healthy individuals were enrolled. Their healthy status was determined by self-reported negative answers to disqualifying neurological and MR contraindications before the scan and an unremarkable MRI determined by a neuroradiologist afterwards. All were briefed on the procedure and provided an Institutional Review Board approved written informed consent.

MR data acquisition

All experiments were carried out on a 3 T scanner (Trio, Siemens AG, Erlangen, Germany) with a TEM3000 circularly-polarized transmit-receive head-coil (MR-Instruments, Minneapolis, MN, USA) capable of delivering a 1 kHz B_1 field to the human head with ~ 1.5 kW of radio-frequency (RF) power. For ^{1}H-MRSI VOI image-guidance and tissue segmentation, 160 1-mm thick slices were acquired by sagittal Magnetization Prepared RApid Gradient Echo (MP-RAGE): $TE/TI/TR = 2.6/800/1360$ ms, 256×256 mm^2 field of view, 256×256 matrix. They were reconstructed in axial, sagittal and coronal planes at 1 mm^3 isotropic resolution and angled to render the genu and splenium of the corpus callosum in the same horizontal plane as shown in Figure 1.

Our chemical-shift imaging-based (CSI) automatic procedure then adjusted the full second order shims in 3–5 minutes (16). Next, a 10-cm anterior-posterior (AP) $\times$ 8 cm left-right (LR) $\times$ 4.5 cm inferior-superior (IS) = 360 cm^3 VOI was image-guided over the corpus callosum as shown in Figure 1. It was excited with a $TE = 35$ ms PRESS in three second-order Hadamard-encoded 1.5 cm thick slabs (for a total of 6 slices) and interleaved along the IS direction every $TR = 1800$ ms (Fig. 1a) for optimal SNR and spatial coverage (17). It also enabled a strong 6 mT/m slice-select gradient for the 5.12 ms Hadamard PRESS 90° RF pulses, reducing the 1.56 ppm (~ 200 Hz) chemical shift between NAA and *m*I to just an ~ 0.6 mm displacement (18). The slices were partitioned with 16×16 CSI over a 16×16 cm^2 FOV to yield $1.0 \times 1.0 \times 0.75$ cm^3 voxels [$1.2 \times 1.2 \times 0.75 \approx 1.1$ cm^3 given the full-width at half-max of the 2D point spread function (19–21)]. The 8×10 cm VOI was defined with two 11.2 ms numerically optimized 180° RF pulses (4.5 kHz bandwidth) under 1.34 (LR) and 1.1 mT/m (AP) gradients to yield $8 \times 10 \times 6 = 480$ voxels. The PRESS 180° RF pulses were calibrated to ensure that their transition bands fell outside the VOI in voxels that were subsequently discarded during post-processing. The MR signal was acquired for 256 ms at 1 kHz bandwidth. At two averages, the ^{1}H-MRSI took 34 min.

Voxel volumetry

Each subject's MP-RAGE images were segmented using SPM2 [Wellcome Department of Cognitive Neurology, Institute of Neurology, Queen Square, London, UK (22,23)] into CSF, WM and GM masks in ~ 15 min on a Core *i*7 class workstation. These were co-registered with the ^{1}H-MRSI grid using in-house software that computed their volume in every *j*-th voxel of the

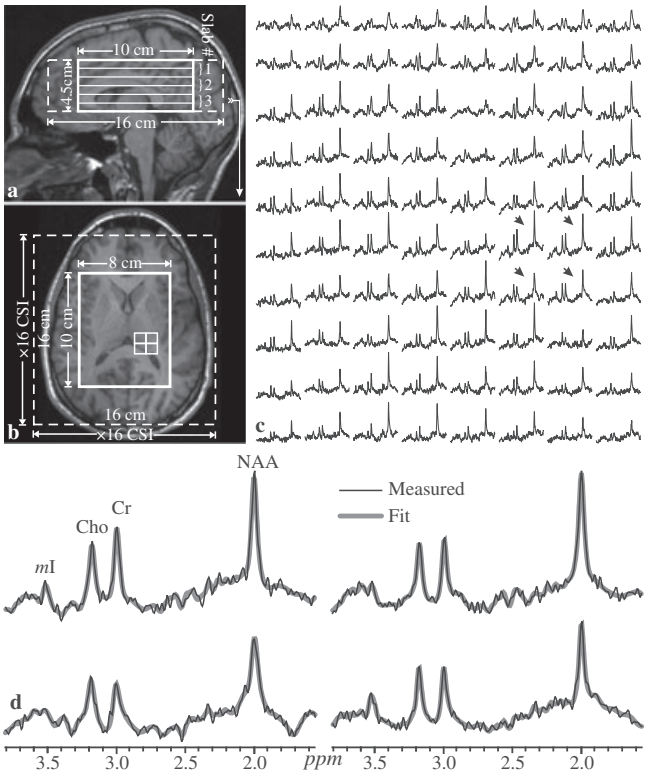

Figure 1. Left: Sagittal (a) and axial (b) T_1-weighted MP-RAGE MRI of subject # 18 in Table 1 superimposed with the $8 \times 10 \times 4.5$ cm^3 VOI, $16 \times 16 \times 4.5$ cm^3 FOV (thick and dashed white frames) and 3 second-order 1.5 cm thick Hadamard slabs (six 0.75 cm thick ^{1}H-MRSI slices) every *TR*. Arrow on (a) indicates the location of (b). Right: (c) Real part of the 8×10 ^{1}H spectra matrix from the VOI on (b) on common 1.7 – 3.7 ppm and intensity scales. Bottom: (d) The 4 spectra from the 2×2 white grid on (b) indicated by the black arrows on (c) are expanded for greater detail, superimposed with the fitted waveform used for quantification in Equation [1]. Note the SNR and spectral resolution from these 0.75 cm^3 voxels in ~ 30 minutes of acquisition and the fit quality.

k-th subject (V_{jk}^{GM}, V_{jk}^{WM}, V_{jk}^{CSF}) in ~ 5 seconds as shown in Figure 2. Since ^{1}H-MRSI and MRI were acquired in the same frame of reference, no deformations or shearing transformations were needed.

Metabolic quantification

^{1}H-MRS data were processed offline using in-house software. Data were voxel-shifted to align the NAA grid with the VOI, then Fourier transformed in time, AP and LR directions and Hadamard-transformed along the IS dimension. Each spectrum was frequency-aligned and zero-order phased in reference to the NAA peak. Relative levels of the *i*-th (i = NAA, Cr, Cho, *m*I) metabolite in the *j*-th ($j = 1 \ldots 480$) voxel in the *k*-th ($k = 1 \ldots 18$) subject S_{ijk} were estimated from their peak area using SITools-FITT spectral modeling software (24). It used the full lineshapes of aspartate, glutamate, glutamine, Cho, Cr, *m*I, NAA and taurine as model functions obtained with the GAVA simulation program for our pulse sequence (25). This process, which takes about 30 min, uses *a priori* spectral information and includes non-parametric baseline signal component characterization and Lorenz-Gauss lineshape assumption. Analysis of this baseline modeling showed that for spectra with 5 Hz linewidth, the mean errors of the fit were 3.4%, 2.3% and 2.8% for NAA, Cr and Cho, respectively (26). The S_{ijk}-s were

scaled into absolute amounts Q_{ijk} against a 2 L sphere of C_i^{vitro} = 12.5, 10.0, 3.0 and 7.5 mM NAA, Cr, Cho and *m*I in water at physiological ionic strength to load the coil and VOI size and position similar to *in vivo* studies to approximate a similar B_1 profile up to the intrinsic differences between the phantom and the head due to tissue–RF field interactions at 3 T:

$$Q_{ijk} = \frac{C_i^{vitro}}{V} \cdot \frac{S_{ijk}}{S_{ijR}} \cdot \left(\frac{P_k^{180^\circ}}{P_R^{180^\circ}} \right)^{1/2} \cdot f_i \quad \text{millimoles}, \qquad [1]$$

where V is the voxel volume (0.75 cm^3); S_{ijR} is the sphere voxel metabolite signal; and $P_k^{180^\circ}$ and $P_R^{180^\circ}$ are the RF power for a non-selective 1 ms 180° inversion pulse on the *k*-th subject and reference. To account for different relaxation times *in vivo* (T_1^{vivo}, T_2^{vivo}) and in the phantom (T_1^{vitro}, T_2^{vitro}), the Q_{ijk} in were corrected for each metabolite *i* using Equation [2] (27):

$$f_i = \frac{\exp\left(-TE/T_2^{vitro}\right)}{\exp\left(-TE/T_2^{vivo}\right)} \cdot \frac{1 - \exp\left(-TR/T_1^{vitro}\right)}{1 - \exp\left(-TR/T_1^{vivo}\right)}. \qquad [2]$$

Global VOI concentrations

Individual age-adjusted T_2^{vivo} WM and GM values for NAA, Cr and Cho were calculated using published formulae (28). For the whole VOI, we used their WM and GM values weighted by each tissue volume fraction in that individual's VOI (sum of their fractions in all the voxels). Their mean T_2^{vivo} values over all 18 subjects were 350, 174 and 251 ms. T_2^{vivo} = 200 ms was used for *m*I with no GM/WM or age difference (29). Since no significant GM/WM or age differences were reported for T_1^{vivo} at 3 T, we used 1360, 1300, 1145 and 1170 ms (29,30). The corresponding values measured in the phantom were T_2^{vitro} = 483, 288, 200, 233 ms and T_1^{vitro} = 605, 336, 235 and 280 ms. The average whole-VOI tissue concentration for each metabolite C_{ik} was obtained by Equation [3]:

$$C_{ik} = \frac{\sum_{j=1}^{480} Q_{ijk}}{\sum_{j=1}^{480} \left(V_{jk}^{GM} + V_{jk}^{WM} \right)} \quad \text{mM/g wet weight}. \qquad [3]$$

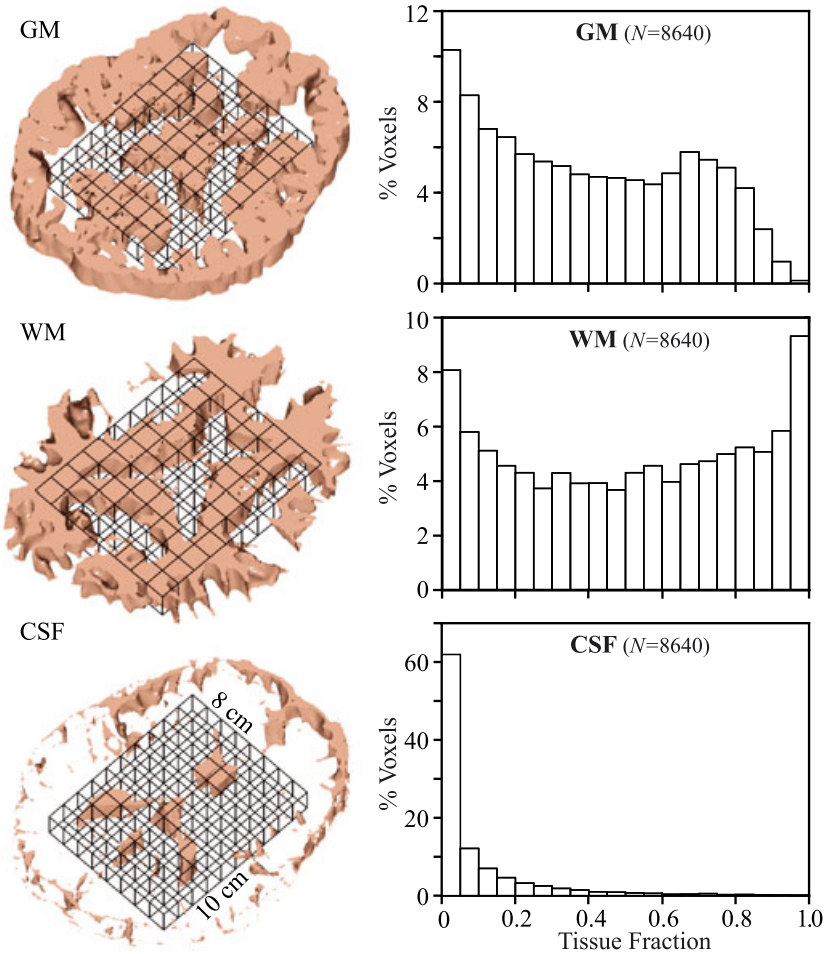

Figure 2. Left: 3D renderings of a single 7.5 mm thick ^{1}H-MRSI slice (black solid grid of 6 in subject # 18) co-registered with its 7.5 corresponding CSF, WM and GM masks (1 mm thick each) segmented from the T1-weighted MP-RAGE with SPM2. Our in-house software counted the number of pixels of each mask fell into every *j*-th MRSI voxel in the VOI to estimate its V_{jk}^{GM}, V_{jk}^{WM}, V_{jk}^{CSF} for the analysis of Equations [3] and [4]. Right: Histograms of the % of the total number of 8,640 voxels (18 subjects × 480 voxels each) containing a given fraction of GM, WM and CSF at 5% bin resolution. Note that even at this relatively high spatial resolution (0.75 cm^3), it is hard to get a "pure", i.e. > 95% WM voxel, a requirement satisfied by less that 10% of all voxels and nearly impossible (<1%) to get one that is > 95% GM.

This sum has the advantage of (number of voxels)$^{1/2}$ ≈ 22 fold less variance than individual elements and consequently, expected to yield better precision, as described by Kreis (4).

Global WM and GM concentrations

Since CSF does not contribute to the ^{1}H-MRS signal, the *i*-th metabolite amount in the *j*-th voxel of the *k*-th subject can be modeled as a sum of two (GM, WM) compartments by Equation [4]:

$$Q_{ijk} = Q_{ijk}^{GM} \cdot f_i^{GM} + Q_{ijk}^{WM} \cdot f_i^{WM} = C_{ik}^{GM} \cdot V_{jk}^{GM} \cdot f_i^{GM} + C_{ik}^{GM} \cdot V_{jk}^{WM} \cdot f_i^{WM}, \quad [4]$$

where C_{ik}^{WM}, C_{ik}^{GM} are the unknown global WM and GM concentrations of the *i*-th metabolite in the *k*-th subject, and f_i^{GM}, f_i^{WM} are calculated by Equation [2] using GM T_2^{vivo}s of 275, 157, 241 and 200 ms for NAA, Cr, Cho and *m*I, and 400, 185, 258 and 200 ms for WM (28,29). The corresponding T_1^{vivo}s, T_2^{vitro}s and T_1^{vitro}s, are the same as for Equation [3]. For each volunteer, Equation [4] comprises a set of 480 over determined equations for C_{ik}^{WM} and C_{ik}^{GM} that can be solved with least-squares optimization that minimizes the total error as per Equation [5]

$$E_{ik}^2 = \sum_{j=1}^{480} E_{ijk}^2 \equiv \sum_{j=1}^{480} \left(C_{ik}^{GM} \cdot V_{jk}^{GM} + C_{ik}^{GM} \cdot V_{jk}^{WM} - Q_{ijk} \right)^2 \quad [5]$$

for each metabolite *i* and patient *k*. Since the brain's GM and WM spatial heterogeneity is on a scale smaller than the 1 cm^3 of the voxels, the $j = 1, \ldots, 480$ V_{jk}^{GM} and V_{jk}^{WM} coefficients (480 equations) are independent, guaranteeing a non-degenerate solution.

RESULTS

Our shim produced a consistent 22 ± 3 Hz FWHM VOI water linewidth. An example of the VOI size, position and ^{1}H-MRSI is shown in Figure 1. The SNRs in 8,640 voxels (18 subjects × 480 voxels each) were: NAA = 30 ± 6, Cr = 15 ± 3, Cho = 13 ± 2 and *m*I = 8 ± 1 (mean ± standard deviation) estimated as peak height divided by twice the root-mean-square of the noise. The metabolites' voxel FWHM linewidth was 6.6 ± 1.1 Hz. The average VOI composition was 9 ± 2% CSF, 39 ± 2% GM and 52 ± 3% WM. Its tissue fraction was 43 ± 2% GM and 57 ± 2% WM. Analysis of the individual voxels' GM, WM and CSF composition (Fig. 2) reveals that even at this relatively high spatial resolution, less than 1% of the voxels can be considered "pure" (95% or greater) GM and under 10% "pure" WM, as shown in Figure 2. Of the 8640 voxels in the 18 VOIs, about 86% contained less than 10% CSF (Fig. 2).

Global VOI, WM and GM metabolites' concentrations from our 18 subjects are compiled in Table 1 with their least-squares errors (E_{ik} in Equation [5]) as quantitative "goodness of the fit" metric. To demonstrate their different GM and WM distributions and sensitivity gain from the segmentation process, the concentrations are also plotted in Figure 3. The absolute-valued NAA residual error map obtained by subtracting the synthesized NAA map (Q_{ijk} calculated from Equation [4] for each voxel using its V_{jk}^{GM} and V_{jk}^{WM} and the global least-squares C_{ik}^{WM}, C_{ik}^{GM}) from the experimental one is

Table 1. Absolute mM whole-VOI tissue concentrations (VOI), global WM and GM concentrations (C^{WM}, C^{GM}) of the NAA, Cho, Cr, mI for the 18 subjects using Equations [3],[4] and least-squares fitting. The global fitting error (E_{ik} in Equation [5]) per voxel (divided by the number of terms in the sum) were calculated for each patient and metabolite and averaged over all patients. The results are (mean ± SD): NAA = 0.11 ± 0.1, Cho = 0.03 ± 0.01, Cr = 0.08 ± 0.01, mI = 0.08 ± 0.08

Subject	Concentrations [mM]											
	NAA			Cr			Cho			mI		
	VOI	C^{WM}	C^{GM}	VOI	C^{WM}	C^{GM}	VOI	C^{WM}	C^{GM}	VOI	C^{WM}	C^{GM}
1	7.2	7.1	8.0	5.4	4.9	6.4	1.4	1.5	1.1	4.6	4.2	5.4
2	8.3	8.3	9.3	6.7	5.0	7.3	1.4	1.5	1.3	4.3	3.9	5.3
3	7.9	7.9	9.1	5.9	4.9	8.1	1.3	1.4	1.3	4.8	4.6	5.7
4	7.5	7.5	8.4	5.1	4.3	6.7	1.2	1.3	1.2	4.6	4.1	5.8
5	7.6	7.2	9.0	5.0	4.5	6.2	1.3	1.4	1.3	4.9	4.8	5.4
6	7.7	7.7	8.3	5.4	4.9	6.6	1.3	1.4	1.3	5.8	5.5	6.5
7	7.0	6.6	8.0	5.0	4.3	6.0	1.0	1.0	1.1	4.2	4.0	4.7
8	7.1	7.7	7.3	4.6	4.4	5.5	1.2	1.3	1.1	6.0	5.9	6.6
9	8.7	8.7	9.4	6.0	5.5	7.0	1.2	1.2	1.1	5.3	5.2	5.8
10	7.6	7.7	8.0	5.6	4.8	6.9	1.3	1.4	1.3	4.4	4.3	4.7
11	7.0	7.2	7.6	5.0	4.6	6.2	1.1	1.2	1.0	4.5	4.7	4.5
12	7.9	8.1	8.3	5.7	5.2	6.9	1.3	1.4	1.3	4.8	4.6	5.4
13	8.4	7.9	9.3	5.3	4.3	6.7	1.3	1.3	1.2	4.4	3.4	5.7
14	7.6	7.6	8.1	5.4	4.4	7.2	1.3	1.2	1.4	4.9	4.5	5.6
15	7.1	7.3	7.1	4.9	4.3	6.2	1.1	1.3	0.9	3.5	3.3	3.9
16	7.8	7.2	9.1	5.9	5.2	7.2	1.4	1.4	1.4	5.1	4.8	5.6
17	8.4	8.4	8.4	6.0	5.6	6.6	1.3	1.5	0.9	4.9	5.1	4.4
18	7.7	7.5	8.7	6.2	5.5	7.5	1.5	1.8	1.2	5.2	5.2	5.4
Mean	7.7	7.6	8.4	5.5	4.8	6.7	1.3	1.4	1.2	4.8	4.6	5.4
SD	0.5	0.5	0.7	0.5	0.4	0.6	0.1	0.2	0.2	0.6	0.7	0.7
CV	7%	7%	8%	8%	9%	9%	10%	13%	13%	12%	15%	13%

NMR IN BIOMEDICINE

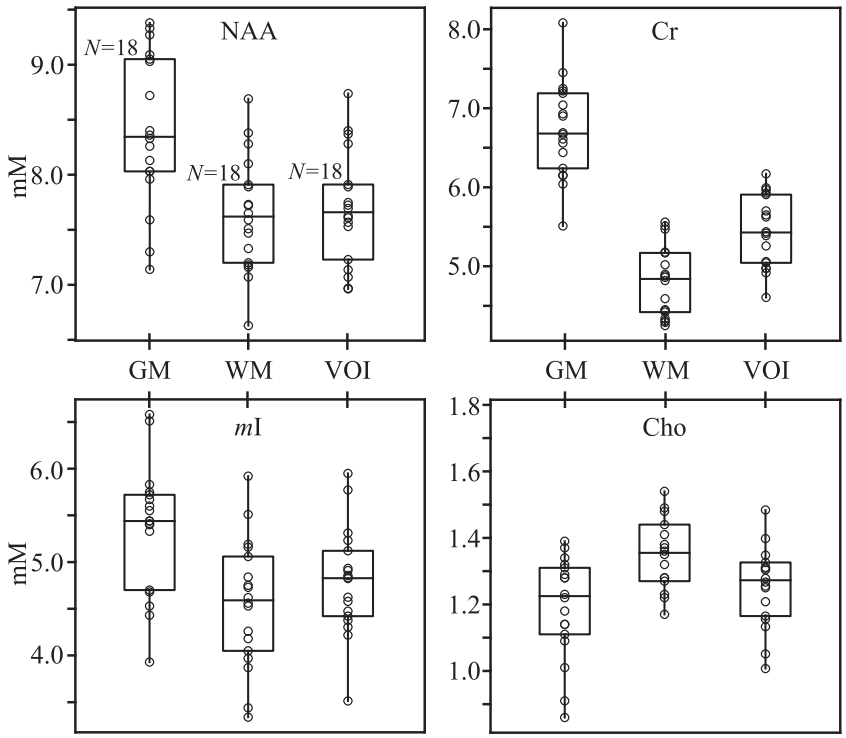

Figure 3. Box plots showing the first, second (median) and third quartiles (box) and ± 95% (whiskers) of the non-tissue specific WM and GM NAA, Cho, Cr and mI whole-VOI concentration distributions superimposed with their respective dot plots showing the concentrations in each for the 18 healthy volunteers. Note the differences between WM and GM tissue-specific concentration differences that can modulate the non-specific VOI concentration depending on their partial-volume, as described by Equations [8] and [9]

shown in Figure 4. Also shown is the normal probability plot for the E_{ik}s for the whole VOI for that metabolite and patient for visual assessment of the statistical normalcy of the errors.

DISCUSSION

The problem of inferring WM and GM-specific metabolite concentrations has been addressed in many ^{1}H-MRS studies. Although single voxel ^{1}H-MRS studies often attempt to circumvent this issue by placing the VOI in "mostly" WM or GM (31), partial volume effects quantified in Figure 2, SNR limitations, and misregistration all introduce quantification errors. A remedy in ^{1}H-MRSI is to apply linear regression to the metabolites' concentrations and either the GM or WM voxel volume fractions (13,32–37). In such linear model, the voxels' signals are assumed to be of the form given by Equation [4], while the constraint $V_{jk}^{GM}+V_{jk}^{WM}+V_{jk}^{CSF}=V$ is addressed by - dividing Q_{ijk} by V - $V_{jk}^{CSF}=V_{jk}^{GM}+V_{jk}^{WM}$; the voxels' signals are then fitted to a straight line of the form:

$$Q_{ijk}=\frac{V_{jk}^{WM}}{V_{jk}^{WM}+V_{jk}^{GM}}C^{WM}+\left(1-\frac{V_{jk}^{WM}}{V_{jk}^{WM}+V_{jk}^{GM}}\right)C^{GM}. \qquad [6]$$

In contrast, minimizing the error given by Equation [5] seeks to fit the data to a 2D plane constrained to pass through the origin: $Q_{ijk}=0$ for $V_{jk}^{WM}=V_{jk}^{GM}=0$. While both approaches are equivalent for a noiseless signal, once a random normally distributed error term (ε_{ijk}) is added to the model (Equation [4]), its division by (V-V_{jk}^{CSF}) raises the variance of the statistical estimators for C^{GM}, C^{WM} (38) by the ratio of the variances of the undivided and divided errors as shown in Equation [4]:

$$\frac{\sum_{ijk}\varepsilon_{ijk}^2}{\sum_{ijk}\left(\varepsilon_{ijk}/\left(\frac{V-V_{jk}^{CSF}}{V}\right)\right)^2}. \qquad [7]$$

This effect can be mitigated by increasing the number of voxels and by excluding all those above a certain threshold for V_{jk}^{CSF}. This, however, may become prohibitive for smaller structures or 2D MRSI data. It can be avoided altogether by employing a 2D constrained fitting procedure (Equation [5]), where division by V-V_{jk}^{CSF} is unnecessary.

Two other studies applied linear regression in sub-structures: e.g. the right temporal lobe (33,34). While concentrations variation among structures is well documented (13,15), arguably in diffuse (or multi-focal) diseases affecting the whole brain, changes are of interest not absolute magnitudes. Applying Equation [4] to the entire heterogeneous VOI therefore, should not detract from the method's power to detect this change and only serves to increase the sensitivity (3,4).

While the improved SNR of this approach is reflected in small 7–15% coefficients of variations (CV = standard deviation/mean) of the C_i^{GM}s and C_i^{WM}s in Table 1, the partial volume confounds are more subtle and will be treated separately. First, random GM and WM voxel composition due to either *(i)* contamination of an intended "pure" tissue or *(ii)* misregistration in different exams may lead to variations in the MRS signal, reducing statistical power to detect pathology-induced changes. Second, these variations also decrease the ability to detect changes specific to one tissue type but not the other.

Quantification errors from partial volume variation

To estimate the error introduced by WM and GM voxel composition variations due to misregistration (scenario *(i)* above), let

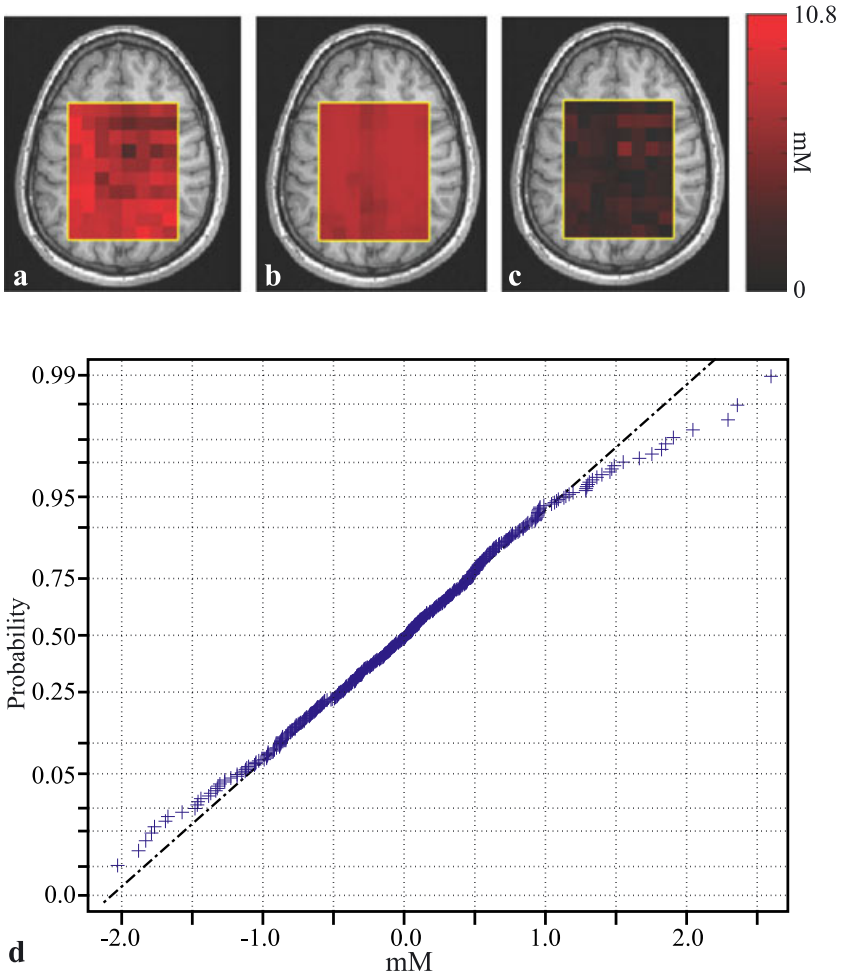

Figure 4. (a) Top left a: the distribution of Q_{ijk} (I = NAA) in spectroscopic slice # 4 (of 6) in subject # 18 in Table 1. Center b: the modeled NAA distribution $\hat{C}_{ik}^{GM} \times V_{jk}^{GM} + \hat{C}_{ik}^{GM} \times V_{jk}^{WM}$ in the same slice reconstructed *a posteriori* using the global least-squares WM and GM concentrations $\hat{C}_{ik}^{WM}$, $\hat{C}_{ik}^{GM}$. Right c: the absolute value of the difference maps on |a – b| showing the residual errors. Note the small residual values on c, demonstrating the quality of the global concentration assumption. Bottom d: A normal probability plot for the error residuals from the entire VOI of that subject. Note that most voxels lie on the (dashed - dot) line indicating a normal distribution, providing visual indication of the normal distribution of the residuals.

V^{WM}, V^{GM} and V be the WM, GM and total voxel (assume for simplicity no CSF: $V = V^{WM} + V^{GM}$) and C^{WM}, C^{GM} the tissue metabolite concentration. This metabolite's ^{1}H-MRS signal from that voxel will be proportional to its amount: $Q = V^{WM} \cdot C^{WM} + V^{GM} \cdot C^{GM}$. Ideally, for a pure WM, one would have $V^{GM} = 0$. However, if the voxel contained unintentional $V^{GM} \neq 0$, then its signal would differ by a multiplicative "fractional error" factor δ:

$$\delta = \frac{C^{WM} \cdot V^{WM} + C^{GM} \cdot V^{GM}}{V \cdot C^{WM}} \quad (\delta = 1 \text{ indicates no error}). \quad [8]$$
$$= 1 + \frac{V^{GM}}{V} \cdot \frac{C^{GM} - C^{WM}}{C^{WM}}$$

Using the median $C^{GM} = 6.7$ mM and $C^{WM} = 4.7$ mM for Cr (often used as an internal standard in ^{1}H-MRS) from Figure 3 and assuming a commonly encountered $V^{GM}/V = 0.2$ – difficult to avoid for large(r) single-voxel studies (Fig. 2) - yields $\delta \approx 1.1$. Thus, the apparent Cr C^{WM} would be biased ~ 10% upwards.

Note that Equation [8] holds true for any change from an initial V^{GM}/V on subsequent measurements (scenario *(ii)* above). Specifically, an easily incurred 20% WM and GM voxel composition difference due to misregistration can lead to quantification variations of the order of 10% for absolute quantification and even more for metabolite ratios (39).

WM and GM specificity loss due to partial volume variation

The MRSI signal of each metabolite in every voxel represents the sum of its GM and WM contributions. However, if a diffuse disease affects the concentration of a metabolite predominantly in GM, e.g. in cognitive disorders or WM, e.g. in leukodystrophies, these tissue-specific changes will be "diluted" and modulated by the signal from the other unaffected tissue fractions, reducing the contrast between patients and controls and, consequently, the sensitivity.

To estimate the magnitude of this contrast loss, consider a diffuse disease that alters only a metabolite's GM concentration C^{GM} by an amount ΔC^{GM}. Denoting that metabolite's overall (unsegmented) concentration in controls by C_{ctrl}, its concentration in patients C_{pts} will be:

$$\begin{aligned} C_{pts} &= \frac{1}{V_{VOI}}\sum_{j=1}^{480} Q_j \\ &= \frac{1}{V_{VOI}}\sum_{j=1}^{480}\left[\left(C_j^{GM}+\Delta C^{GM}\right)\cdot V_j^{GM}+C_j^{WM}\cdot V_j^{WM}\right] \\ &= C_{ctrl}+\Delta C^{GM}\cdot\frac{V_{VOI}^{GM}}{V_{VOI}} \end{aligned} \quad [9]$$

where the metabolite (i) and patient (k) indices were omitted for brevity and V_{VOI}^{GM}, V_{VOI}^{WM}, V_{VOI} ($= V_{VOI}^{GM} + V_{VOI}^{WM}$) are the total GM, WM and VOI tissue volumes. The observed global change in that metabolites' concentrations will be V^{GM}/V smaller than the true change ΔC^{GM}, since V^{GM}/V (or for that matter V^{WM}/V) is always ‹1, reflecting a loss of both tissue specificity and sensitivity.

The consequences of such a loss can be estimated by assuming the GM and WM metabolites' concentrations are homogeneous within each patient and normally distributed in both controls and patients: $C_{pts}^{GM} \sim N\left(\mu_{pts}^{GM}, \sigma^{GM}\right)$, $C_{\mathrm{pts}}^{WM} \sim N\left(\mu_{pts}^{WM}, \sigma^{WM}\right)$ and $C_{\mathrm{ctrl}}^{GM} \sim N\left(\mu_{ctrl}^{GM}, \sigma^{GM}\right)$ $C_{\mathrm{ctrl}}^{WM} \sim N\left(\mu_{ctrl}^{WM}, \sigma^{WM}\right)$, where $\mu_{pts}^{GM} = \mu_{ctrl}^{GM} + \Delta C^{GM}$ and $\mu_{ctrl}^{WM} = \mu_{pts}^{WM} \equiv \mu^{WM}$ since the pathology does not alter the WM concentrations. Here, $N(\mu,\sigma)$ symbolizes a normal distribution having mean μ and standard deviation σ. We also assume to first order that the pathology only alters the means not the standard deviations of the GM distributions. The number of patients needed to observe a change ΔC^{GM} in a GM only VOI with 80% power and a two-sided significance level of 0.05 is given by Equation [10] (38):

$$N_{segmented} \geq \left[\frac{2.8\sqrt{2}\sigma^{GM}}{\Delta C^{GM}}\right]^2. \quad [10]$$

The global non tissue-specific concentration of a metabolite in question C_{ctrl} is given by the weighted average of its tissue concentrations $C_{ctrl} = f_{VOI}^{GM}\cdot C_{VOI}^{GM} + f_{VOI}^{WM}\cdot C_{VOI}^{WM}$, where $0 \leq f_{VOI}^{GM}$ and $f_{VOI}^{WM} \leq 1$ are the VOI GM and WM fractions. Thus, C_{ctrl}, C_{pts} are also normally distributed:

$$\begin{aligned} C_{ctrl} &\sim N\left(f_{VOI}^{WM}\mu^{WM} + f_{VOI}^{GM}\mu_{ctrl}^{GM}, \sqrt{\left(f_{VOI}^{WM}\sigma^{WM}\right)^2 + \left(f_{VOI}^{GM}\sigma^{GM}\right)^2}\right) \\ C_{pts} &\sim N\left(f_{VOI}^{WM}\mu^{WM} + f_{VOI}^{GM}\mu_{ctrl}^{GM} + f_{VOI}^{GM}\Delta C^{GM}, \sqrt{\left(f_{VOI}^{WM}\sigma^{WM}\right)^2 + \left(f_{VOI}^{GM}\sigma^{GM}\right)^2}\right) \end{aligned} \quad [11]$$

The number of patients needed to observe this difference with the same statistical power (80%) and significance level (0.05) as before has now increased:

$$N_{non-segmented} \geq \left[\frac{2.8\sqrt{2\left(f_{VOI}^{WM}\sigma^{WM}\right)^2 + 2\left(f_{VOI}^{GM}\sigma^{GM}\right)^2}}{f_{VOI}^{GM}\Delta C^{GM}}\right]^2. \quad [12]$$

For example, in the VOIs studied herein, the WM:GM $\approx$ 3 : 2. Given whole-brain WM : GM of ~ 0.7 (40,41), $f_{VOI}^{WM} \approx f_{VOI}^{GM} \approx 0.5$ is a reasonable first order approximation in any VOI large enough to observe diffuse metabolic changes. Furthermore, Table 1 reveals that for most metabolites, $\sigma^{GM} \approx \sigma^{WM}$. Substituting into Equation [12] yields:

$$N_{\text{non-segmented}} \geq 2N_{\text{segmented}}. \quad [13]$$

Equation [13] represents a general rule of thumb for any sufficiently large heterogeneous VOI: A linear regression like the one described can increase a study's statistical power two-fold.

Applications

The method described in this review is applicable in the following clinical scenarios: (*i*) In diseases with a known diffuse component such as traumatic brain injury, multiple sclerosis, encephalopathies, late stage dementias and HIV-associated neurological disorder, tumours and leukodystrophies (in those diseases with focal centers, the method can be used to observe the diffuse component in the adjacent normal appearing tissue); (*ii*) In focal disease where a hypothesis tests for diffuse involvement of normal-appearing tissue; (*iii*) In focal disease known to advance to diffuse (e.g. dementias) in order to time the progression; and (*iv*) in both diffuse and focal diseases to assess global drug effects.

Caveats

Global WM and GM quantification is subject to several limitations arising from an approach geared to maximize sensitivity at the expense of localization. *(i)* It is insensitive to focal changes that may occur in specific small brain regions. *(ii)* Since metabolites' concentrations are assumed to be the same in a given tissue type (GM or WM), only uniform diffuse changes (all increases or all decreases) are detectable. Large changes in concentrations between brain structures within a particular tissue - e.g. between the cerebrum and cerebellum (42) - will be averaged out, which will diminish the approach's statistical power. This limitation, however, can be relaxed since, although we used 480 equations (Equation [4]) to deduce C^{WM}, C^{GM}, only two equations are actually necessary. The other 480 – 2 = 478 merely increase the robustness. Therefore, if the VOI is divided into sub-regions of at least 2 voxels each, their local C^{WM} and C^{GM} could be determined on a spatial scale only slightly coarser than the acquisition grid. *(iii)* Long post-processing (~ 45 min/subject) may impede clinical application. Finally, *(iv)* although our VOI covered substantially more brain than most single voxel or 2D ^{1}H-MRSI studies, it excluded most of the cortex and infratentorial brain. Given the average brain GM and WM volumes of ~ 700 cm^3 and 500 cm^3 (41) our VOI contained 20% of the total GM (including cortical and most of the deep structures) and 40% of the WM. The cortical periphery was excluded due to technical challenges of cortical spectroscopy, including lipid contamination and shimming artifacts. However, given a multivoxel sequence capable of overcoming these limitations, the cortex would make an excellent candidate for investigation using this technique: the tortuous thin (1–4 mm) GM cortical strip is often impossible to observe directly with multivoxel spectroscopy due to the large spectroscopic voxels and the partial volume effects from the adjacent white matter. A linear regression-based method such as the one described herein, in combination with the excellent performance of most segmentation algorithms for the other regions of the brain, can be used to obtain cortex-specific spectra. Given the functional and cognitive importance of the cortical GM, we anticipate the outlined approach to become a useful tool for probing cortical GM metabolite concentrations.

CONCLUSIONS

Although ^{1}H-MRSI can yield spatial distribution maps of brain metabolites, these often do not come at sufficient SNR (sensitivity) to identify small changes incurred in diffuse pathologies. One of the controllable factors that lowers the sensitivity is voxel tissue partial volume variations. Readily available segmentation software in conjunction with anatomical MRI allows us now to leverage the myriad ^{1}H-MRSI voxels to obtain global tissue-specific metabolite concentrations. The process also dramatically $\propto$ (number of voxels)$^{1/2}$ increases the precision and by its nature addresses the WM, GM and CSF partial volume metabolic quantification variations issue encountered in ^{1}H-MRSI. Together, these may allow the detection of smaller metabolic changes with greater statistical power and better assign them to pathologies that may preferentially target the GM, WM or both, leading to higher sensitivity and consequently fewer patients (or measurements) needed to determine a change. Finally, note that this improvement is "free": i.e. achieved entirely in post-processing with no additional demands of the measurement time, protocol or hardware.

Acknowledgements

This work was supported by NIH Grants EB01015, NS050520, NS39135 and NS29029. Assaf Tal acknowledges the support of the Human Frontiers Science Project.

REFERENCES

1 Mountford CE, Stanwell P, Lin A, Ramadan S, Ross B. Neurospectroscopy: the past, present and future. Chem. Rev. 2010; 110(5): 3060–3086.
2 Tran T, Ross B, Lin A. Magnetic resonance spectroscopy in neurological diagnosis. Neurol. Clin. 2009; 27(1): 21–60.
3 Kirov II, George IC, Jayawickrama N, Babb JS, Perry NN, Gonen O. Longitudinal inter- and intra-individual human brain metabolic quantification over 3 years with proton MR spectroscopy at 3 T. Magn. Reson. Med. 2011; 67(1): 27–33.
4 Kreis R, Slotboom J, Hofmann L, Boesch C. Integrated data acquisition and processing to determine metabolite contents, relaxation times, and macromolecule baseline in single examinations of individual subjects. Magn. Reson. Med. 2005; 54(4): 761–768.
5 Kreis R. Quantitative localized 1H MR spectroscopy for clinical use. Prog. NMR Spectrosc. 1997; 31(2–3): 155–195.
6 Barker PB, Bizzi A, Stefano ND, Gullapalli R, Lin DDM. *Clinical MR Spectroscopy: Techniques and Applications*. Cambridge University Press: Cambridge, 2009.
7 Caramanos Z, Narayanan S, Arnold DL. 1H-MRS quantification of tNA and tCr in patients with multiple sclerosis: a meta-analytic review. Brain 2005; 128(11): 2483–2506.
8 Jansen JF, Backes WH, Nicolay K, Kooi ME. 1H MR spectroscopy of the brain: absolute quantification of metabolites. Radiology 2006; 240(2): 318–332.
9 Li BS, Babb JS, Soher BJ, Maudsley AA, Gonen O. Reproducibility of 3D proton spectroscopy in the human brain. Magn. Reson. Med. 2002; 47 (3): 439–446.
10 Macovski A. Noise in MRI. Magn. Reson. Med. 1996; 36(3): 494–497.
11 Fischl B, Dale AM. Measuring the thickness of the human cerebral cortex from magnetic resonance images. Proc. Natl. Acad. Sci. 2000; 97(20): 11050–11055.
12 Maudsley AA, Domenig C, Sheriff S. Reproducibility of serial whole-brain MR spectroscopic imaging. NMR Biomed. 2010; 23: 251–256.
13 Bonekamp D, Horska A, Jacobs MA, Arslanoglu A, Barker PB. Fast method for brain image segmentation: application to proton magnetic resonance spectroscopic imaging. Magn. Reson. Med. 2005; 54: 1268–1272.
14 Penny WD, Friston KJ, Ashburner JT, Kiebel SJ, Nichols TE. *Statistical Parametric Mapping: The Analysis of Functional Brain Images*. Academic Press: Boston, 2006.
15 Degaonkar MN, Pomper MG, Barker PB. Quantitative proton magnetic resonance spectroscopic imaging: regional variations in the corpus callosum and cortical gray matter. J. Magn. Reson. Imaging 2005; 22(2): 175–179.
16 Hu J, Javaid T, Arias-Mendoza F, Liu Z, McNamara R, Brown TR. A fast, reliable, automatic shimming procedure using 1H chemical-shift-imaging spectroscopy. J. Magn. Res. B. 1995; 108: 213–219.
17 Goelman G, Liu S, Hess D, Gonen O. Optimizing the efficiency of high-field multivoxel spectroscopic imaging by multiplexing in space and time. Magn. Reson. Med. 2006; 56: 34–40.
18 Goelman G, Liu S, Fleysher R, Fleysher L, Grossman RI, Gonen O. Chemical-Shift Artifact Reduction in Hadamard-Encoded MR Spectroscopic Imaging at High (3T and 7T) Magnetic Fields. Magn. Reson. Med. 2007; 58: 167–173.
19 Brooker HR, Mareci TH, Mao JT. Selective Fourier transform localization. Magn. Reson. Med. 1987; 5(5): 417–433.
20 Mareci TH, Brooker HR. Essential Considerations for Spectral Localization Using Indirect Gradient Encoding of Spatial Information. J. Magn. Res. 1991; 92: 229–246.
21 Goelman G, Liu S, Gonen O. Reducing Voxel Bleed in Hadamard Encoded MRI and MRS. Magn. Reson. Med. 2006; 55: 1460–1465.
22 Ashburner JT, Friston KJ. Multimodal image coregistration and partitioning--a unified framework. Neuroimage 1997; 6(3): 209–217.
23 Ashburner JT, Friston KJ. Voxel-based morphometry--the methods. Neuroimage 2000; 11(6): 805–821.
24 Soher BJ, Young K, Govindaraju V, Maudsley AA. Automated spectral analysis III: application to *in vivo* proton MR spectroscopy and spectroscopic imaging. Magn. Reson. Med. 1998; 40(6): 822–831.
25 Soher BJ, Young K, Bernstein A, Aygula Z, Maudsley AA. GAVA: Spectral simulation for in vivo MRS applications. J. Magn. Reson. 2007; 185(2): 291–299.
26 Soher BJ, Young K, Maudsley AA. Representation of strong baseline contributions in 1H MR spectra. Magn. Reson. Med. 2001; 45(6): 966–972.
27 Inglese M, Li BS, Rusinek H, Babb JS, Grossman RI, Gonen O. Diffusely elevated cerebral choline and creatine in relapsing-remitting multiple sclerosis. Magn. Reson. Med. 2003; 50(1): 190–195.
28 Kirov II, Fleysher L, Fleysher R, Patil V, Liu S, Gonen O. Age dependence of regional proton metabolites T2 relaxation times in the human brain at 3T. Magn. Reson. Med. 2008; 60(4): 790–795.
29 Posse S, Otazo R, Caprihan A, Bustillo J, Chen H, Henry PG, Marjanska M, Gasparovic C, Zuo C, Magnotta V, Mueller B, Mullins P, Renshaw P, Ugurbil K, Lim KO, Alger JR. Proton echo-planar spectroscopic imaging of J-coupled resonances in human brain at 3 and 4 Tesla. Magn. Reson. Med. 2007; 58(2): 236–244.
30 Traber F, Block W, Lamerichs R, Gieseke J, Schild HH. 1H metabolite relaxation times at 3.0 tesla: Measurements of T1 and T2 values in normal brain and determination of regional differences in transverse relaxation. J. Magn. Reson. Imag. 2004; 19(5): 537–545.
31 Malucelli E, Manners DN, Testa C, Tonon C, Lodi R, Barbiroli B, Lotti S. Pitfalls and advantages of different strategies for the absolute quantification of N-acetyl aspartate, creatine and choline in white and grey matter by 1H-MRS. NMR Biomed. 2009; 22: 1003–1013.
32 Doyle TJ, Bedell BJ, Narayana PA. Relative concentrations of proton mr visible neurochemicals in gray and white matter in human brain. Magn. Reson. Med. 1995; 33: 755–759.
33 Govind V, Gold S, Kaliannan K, Saigal G, Falcone S, Arheart KL, Harris L, Jagid J, Maudsley AA. Whole-brain proton mr spectroscopic imaging of mild-to-moderate traumatic brain injury and correlation with neuropsychological deficits. J. Neurotrauma 2010; 27: 483–496.
34 Yeo RA, Gasparovic C, Merideth F, Ruhl D, Doezema D, Mayer AR. A longitudinal proton magnetic resonance spectroscopy study of mild traumatic brain injury. J. Neurotrauma 2011; 28: 1–11.
35 Hetherington HP, Pan JW, Mason GF, Adams D, Vaughn MJ, Twieg DB, Pohost GM. Quantitative 1h spectroscopic imaging of human brain at 4.1 T using image segmentation. Magn. Reson. Med. 1996; 36: 21–29.
36 McLean MA, Barker GJ. Concentrations and magnetization transfer ratios of metabolites in gray and white matter. Magn. Reson. Med. 2006; 56: 1365–1370.
37 Pan JW, Twieg DB, Hetherington HP. Quantitative spectroscopic imaging of the human brain. Magn. Reson. Med. 1998; 40: 363–369.
38 Wasserman L. *All of Statistics: A Concise Course in Statistical Inference*. Springer: Berlin, 2010.

39 Li BS, Wang H, Gonen O. Metabolite ratios to assumed stable creatine level may confound the quantification of proton brain MR spectroscopy. Magn. Reson. Imag. 2003; 21(8): 923–928.
40 Herndon RC, Lancaster JL, Giedd JN, Fox PT. Quantification of white matter and gray matter volumes from three dimensional magnetic resonance volume studies using fuzzy classifiers. J. Magn. Reson. Imag. 1998; 8(5): 1097–1105.
41 Ge Y, Grossman RI, Babb JS, Rabin ML, Mannon LJ, Kolson DL. Age-related total gray matter and white matter changes in normal adult brain. Part II: quantitative magnetization transfer ratio histogram analysis. Am. J. Neuroradiol. 2002; 23(8): 1334–1341.
42 Pouwels PJW, Frahm J. Regional metabolite concentrations in human brain as determined by quantitative localized proton MRS. Magn. Reson. Med. 1998; 39(1): 53–60.

